Simulation and Manipulation of Tunable Weyl-Semimetal Bands Using Superconducting Quantum Circuits

Xinsheng Tan,[1] Y. X. Zhao,[1] Qiang Liu,[1] Guangming Xue,[1] Hai-Feng Yu,[1,*] Z. D. Wang,[2,†] and Yang Yu[1,‡]
[1]National Laboratory of Solid State Microstructures, School of Physics, Nanjing University, Nanjing 210093, China
[2]Department of Physics and Center of Theoretical and Computational Physics, The University of Hong Kong, Pokfulam Road, Hong Kong, China

(Received 16 August 2018; published 8 January 2019)

We simulated highly tunable Weyl-semimetal bands using superconducting quantum circuits. Driving the superconducting quantum circuits with microwave fields, we mapped the momentum space of a lattice to the parameter space, realizing the Hamiltonian of a Weyl semimetal. By measuring the energy spectrum, we directly imaged the Weyl points, whose topological winding numbers were further determined from the Berry curvature measurement. In addition, we manipulated the band structure with an additional pump microwave field, producing a momentum-dependent Weyl-point energy together with an artificial magnetic field, which are indispensable for generating chiral magnetic topological currents in some special Weyl semimetals and may have significant impact on topological physics.

DOI: 10.1103/PhysRevLett.122.010501

Topological effects have attracted broad interest because they not only deepen our understanding of fundamental physics but also are promising for realizing robust quantum information processing. Among topological materials, Weyl semimetals (WSMs) form a representative family that possess topologically protected band crossing points, Weyl points [1–3], whose physical properties have recently been addressed extensively [4–8], including negative magnetoresistance effects induced by a so-called chiral anomaly (CA). Although significant progress has been achieved in probing the topological properties of WSMs, many interesting phenomena are still unexplored. For instance, the chiral magnetic effect (CME) [9–11], which arises purely from the topology of paired Weyl points and requires that the two paired points must be separated in both momentum and energy with a magnetic field being applied, has not yet been detected in nature. The main challenge lies in the limited flexibility of engineering and manipulating the WSM band structures in a designated tunable way such that the CME is detectable. In order to maximize the flexibility and then explore more topological effects, here we present a setup for simulating highly tunable Weyl-semimetal bands in condensed matter systems. By driving the superconducting quantum circuits [12,13] with elaborately designed microwaves [14–18], we first realized a Weyl-semimetal band in an artificial system. We measured the spectroscopy, directly imaging the Weyl points, whose monopole charges are further determined by the Berry curvature measurement. Then we applied another microwave field to continuously tune the Weyl-point energy to a well-designed momentum-dependent form. In addition, we derived an equation of the CME topological current in our engineered Weyl-semimetal bands with multiple Weyl pairs, and manipulated the virtual currents determined from this equation by tuning various parameters, demonstrating the full flexibility in manipulating Weyl points and introducing the wanted artificial magnetic field.

A lattice version of a simplified Weyl-semimetal Hamiltonian may be written as

$$H(k) = \sin k_x \sigma_x + \sin k_y \sigma_y + (\lambda + \cos k_z)\sigma_z + u_0(\mathbf{k})\sigma_0, \quad (1)$$

where $\sigma_{x,y,z}$ are the Pauli matrices and σ_0 is the unit matrix. $\mathbf{k}$ (k_x, k_y, k_z) is the momentum (or wave) vector, and λ ($|\lambda| \leq 1$) is an experimentally controllable parameter that determines the k_z coordinates of the Weyl points (band crossing points). In most cases, $u_0(\mathbf{k})$ is zero or a k-independent constant, which merely introduces an extra energy shift. A Weyl point can be considered as a "magnetic monopole" for its associated Berry bundle. Physically, the monopole charge is a generalization of the chirality, and particularly right-handed (left-handed) Weyl point has a positive (negative) unit charge. We here wish to point out that Eq. (1) is a single-particle Hamiltonian, which may be used for describing any kind of single-particle excitations including fermions and bosons. And for a given $\mathbf{k}$, it just corresponds to a particular two-level system with $\mathbf{k}$-dependent parameters. Therefore, the WSM band here can be simulated by a completely tunable qubit system.

In order to simulate the Hamiltonian of WSM bands, we used a three-dimensional superconducting transmon system [18,19]. The transmon, which is composed of a single Josephson junction and two pads (250×500 μm^2), was put in a rectangular aluminum cavity with the resonance frequency of TE101 mode about 9.026 GHz. In our experiments, the main function of the cavity is to control

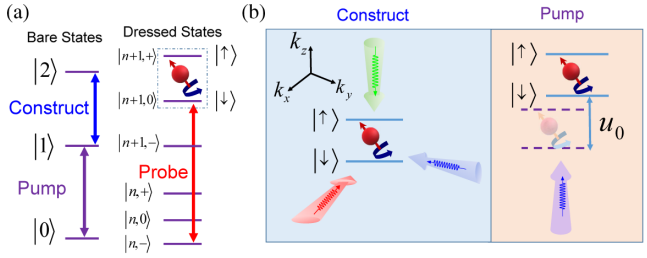

FIG. 1. (a) The energy diagram of a transmon without (left) and with (right) microwave driving. The construct (pump) microwave field is applied to $|1\rangle$ and $|2\rangle$ ($|0\rangle$ and $|1\rangle$). The system transforms to the dressed states, as shown in the right-hand panel. (b) Left: Microwaves with various frequencies, amplitudes, and phases are applied to construct the Hamiltonian. Right: Schematic for the effect of an extra pump microwave field, which is to generate a parameter-dependent energy offset.

and measure the transmon. The system is designed to work in the dispersive regime. The whole sample package was cooled in a dilution refrigerator to a base temperature of 30 mK. The dynamics of the system can be described by the circuit QED theory, which addresses the interaction of an artificial atom with microwave fields [20–23]. The quantum states of the transmon can be controlled by microwaves. In-phase and quadrature mixers combined with a 1 GHz arbitrary wave generator (AWG) were used to modulate the amplitude, frequency, and phase of microwave pulses [24]. The measurement was performed with a "high power readout" scheme [18,30]. As a strong microwave on resonance with the cavity is sent in, the transmitted amplitude of the microwave reflects the state of the transmon due to the nonlinearity of the cavity QED system.

Conventionally, the transmon (coupled with cavity) exhibits anharmonic multiple energy levels. In our experiments, we considered the lowest three bare energy levels of the transmon, as shown in the left-hand part of Fig. 1(a), namely, $|0\rangle$, $|1\rangle$, and $|2\rangle$. The transition frequencies between different energy levels are $\omega_{10}/2\pi = 7.1755$ and $\omega_{21}/2\pi = 6.8310$ GHz, respectively, which were independently calibrated by saturation spectroscopy. To map the transmon Hamiltonian to the form of Eq. (1), we applied construct (pump) microwaves to the transmon, coupling to states $|1\rangle$ and $|2\rangle$ ($|0\rangle$ and $|1\rangle$). The original bare states $|0\rangle$, $|1\rangle$, and $|2\rangle$ will then transform to microwave dressed states [17]. In the right-hand part of Fig. 1(a), we show six relevant dressed states, which are denoted by $|n,-\rangle$, $|n,0\rangle$, $|n,+\rangle$, $|n+1,-\rangle$, $|n+1,0\rangle$, and $|n+1,+\rangle$, respectively. Here n is the average number of photons in the coherent drive. The eigenenergies of these dressed states depend on the microwave fields. In our experiments, the lowest level $|n,-\rangle$ acted as the reference level because the system was always initialized in it. The top two levels $|n+1,+\rangle$ and $|n+1,0\rangle$ were selected as two eigenstates of spin-1/2 atoms. Under microwave driving, the effective Hamiltonian of a spin-1/2 atom in the rotating frame may be written as $\hat{H} = \sum_{i=0}^{3} \Omega_i \sigma_i/2$, ($\hbar = 1$ for simplicity), where Ω_1 (Ω_2) corresponds to the frequency of Rabi oscillations around the x (y) axis on the Bloch sphere, which can be continuously adjusted by changing the amplitude and phase of the construct microwave applied to the system. $\Omega_3 = \omega_{21} - \omega_{\text{construct}}$ is determined by the detuning between the energy level spacing ω_{21} and the construct microwave frequency. Ω_0, corresponding to u_0 in the above Hamiltonian, is related to the energy spacing between $\{|n+1,+\rangle, |n+1,0\rangle\}$, and $|n,-\rangle$. Since the splitting of $|n,-\rangle$ and $|n,+\rangle$ ($|n+1,-\rangle$ and $|n+1,+\rangle$) depends on the frequency and amplitude of the pump (construct) microwave, we can accurately design Ω_0 after calibration [31]. Therefore, by elaborately designing the waveform of AWG and frequencies of microwaves, we can construct every term in the above Hamiltonian point by point. We sent the probe microwave and swept the frequency. When the frequency of the probe microwave matched the energy spacing between $|n,-\rangle$ and $|n+1,+\rangle$ (or $|n+1,0\rangle$), a resonant peak could be observed. By collecting the resonant peaks for various $\mathbf{k}$ parameters, we obtained the band structures of Weyl semimetals [24].

We first demonstrated the realization and manipulation of Weyl-semimetal bands for $u_0(\mathbf{k}) = 0$. In this case, the pump microwave field was actually turned off. The corresponding waveforms were synthesized by AWG and sent to the microwave sources for constructing the Hamiltonian in Eq. (1). Here we set $\Omega_1/2 = \Omega \sin k_x$, $\Omega_2/2 = \Omega \sin k_y$, and $\Omega_3/2 = \Omega(\lambda + \cos k_z)$, with unit $\Omega = 10$ MHz. To visualize the band structure of the Weyl semimetal, we measured the spectroscopy of the lattice Hamiltonian in the first Brillouin zone, as shown in Fig. 2. Weyl points, as the signature of Weyl semimetals, are directly observed. As illustrated in Fig. 2, eight Weyl points are observed in the first Brillouin zone. There are four points with a positive (negative) charge, which are named W_+ (W_-) and denoted by red (green) color. To characterize their topological properties, we also measured the winding number of each Weyl point by detecting the Berry curvature, which was determined by measuring the nonadiabatic response to the change of the external parameter [14–16]. We let the system evolve quasiadiabatically along a designed path in the parameter space, so that the Berry curvature is directly related to $\langle \sigma_y \rangle$ [31]. Then the winding numbers for $W_\pm$ could be obtained by performing quantum state tomography [24]. As shown in Fig. 2(b), the winding number of $W_\pm$ approximates ± 1, close to the predicted value, where $\pm$ of the winding number corresponds to the topological charge sign of Weyl points. Moreover, we can continuously vary λ to explore various topological properties of Weyl semimetals. For instance, we observed that with the change of λ, Weyl points merge and annihilate. Shown in Figs. 2(c)–2(e) are three-dimensional spectra for $\lambda = 0$, -0.5, and -1, from left to right. When $\lambda = 0$, there are eight Weyl points, located at $(0, 0, \pm\pi/2)$,

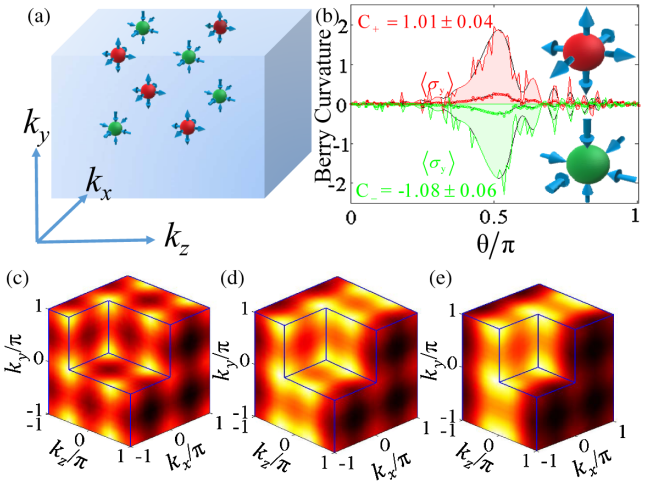

FIG. 2. (a) Illustration of Weyl points in the first Brillouin zone. Weyl points with positive (negative) charges are denoted by red (green) color. (b) Schematic of the formation of winding numbers at a positive (negative) Weyl point. Measured winding number from $\langle\sigma_y\rangle$ are close to $+1$ (-1), corresponding to Weyl points with positive (negative) charges. (c)–(e) Measured three-dimensional energy spectra of the Weyl semimetal in the first Brillion zone for $\lambda = 0, -0.5, -1$. The brightest points are Weyl points with the charges labeled. The locations of gapless Weyl points are found to shift with λ.

$(0, \pi, \pm\pi/2)$, $(\pi, 0, \pm\pi/2)$, and $(\pi, \pi, \pm\pi/2)$, respectively. With λ decreasing from 0 to -1, Weyl points move along the k_z direction. When $\lambda = -1$, the eight Weyl points merge to four Dirac points, which corresponds to a topological phase transition from the topological WSM phase to a normal Dirac metal phase.

Having manipulated the Weyl points in a virtual momentum space, we can demonstrate the further tunability by shifting the energy of the Weyl points, which is mainly motivated by the so-called chiral magnetic effect in WSMs addressed below. According to the Nielsen-Ninomiya no-go theorem [33], these Weyl points always form dipoles, each of which is composed of two oppositely charged monopoles. Thus the electromagnetic response of WSMs lies essentially inside each dipole. Namely, a left-handed Weyl point is separated by b_μ $(\mu = 0, 1, 2, 3)$ from a right-handed one in energy-momentum space. Because of the topological nature of the dipole momentum b_μ, a unique topological term responding exclusively to the magnetic field may be expected from a minimal model of WSM consisting of only one dipole of Weyl points. The corresponding action is given by $S_\Theta = [-(1/8\pi^2)] \int d^4x \epsilon^{\mu\nu\lambda\sigma} b_\mu A_\nu \partial_\lambda A_\sigma$, where A_ν represents the corresponding component of the electromagnetic potential, and $\epsilon^{\mu\nu\lambda\sigma}$ is the Levi-Cività symbol (here the electronic charge is set to $e = 1$ for simplicity) [11,31]. This action leads to the anomalous current $j^\mu = [-(1/8\pi^2)]\epsilon^{\mu\nu\lambda\sigma} b_\nu F_{\lambda\sigma}$, where $F_{\lambda\sigma}$ is the electromagnetic field tensor. A remarkable result is that when two oppositely charged Weyl points are separated by an energy difference b_0, a solely external magnetic field $\mathbf{B}$ is able to induce an additional pure topological current $\mathbf{J}_{\text{topo}}$ given by [31]

$$\mathbf{J}_{\text{topo}} = \frac{b_0}{4\pi^2}\mathbf{B}. \tag{2}$$

This is the equation of CME for one pair of Weyl points. The current arises purely from a topological effect, and is directly proportional to the magnetic field, in contrast to the famous Ampere's law. Notably, this CME topological current is inherently different from the CA currents extensively addressed for WSMs over the past several years [4–8]. Here, the CA and CME currents are respectively originated from the two different topological terms in the action and described by distinct formulas [31]. The topological term in the action with the dipole momentum has the advantage of being readily generalizable to a generic WSM containing multiple dipoles. For a generic case, we need to introduce a modified b_μ for multiple dipoles of monopoles: $b_\mu = \sum_s (K_s^{+,\mu} - K_s^{-,\mu})$, where s labels left- or right-handed Weyl points, and $K_s^{\pm,\mu}$ are the positions of left- or right-handed Weyl points in the energy-momentum space. It follows that CME can still be described by Eq. (2) with the above-introduced modified b_0 [31]. It is noteworthy that the time-reversal symmetry should be broken for a nonvanishing chiral magnetic effect, as seen from Eq. (1); otherwise, the CME current may be vanishing [34].

From Eq. (2), we note that there are two factors that account for CME topological currents. The first is a nonzero b_0, which is difficult to fulfill in real materials, and the second is the presence of a magnetic field. Using our highly tunable Weyl-semimetal bands, we can realize the two factors at the same time by adding additional pump microwave fields, though notably no particle current really occurs in our parametrized single-qubit system. We first show how to obtain a finite b_0 [24]. As shown in Eq. (1), $u_0(\mathbf{k})$ is the prefactor of the σ_0 term. For our WSM, we have four pairs of Weyl points. In an ideal case, b_0 may be 4 times the energy difference between a single pair of W_+ and W_- points. We noticed that the Weyl points have different locations in momentum space. If one can produce a momentum-dependent σ_0 term, the energy difference of the two Weyl points will be nonvanishing. In order to realize a momentum-dependent $u_0(\mathbf{k})$, we applied an extra pump microwave field to shift the reference level for different $\mathbf{k}$. In the dressed state picture, the absolute value of the eigenenergy is determined by the energy spacing between subspace $\{|n+1,+\rangle, |n+1,0\rangle\}$ and $|n,-\rangle$, which is $\omega_{01} + \Delta_{01}/4 + 3\sqrt{\Delta_{01}^2 + \Omega_{01}^2}/4$ in the $E - k_z$ plane which contains Weyl points [31]. Here Δ_{01} is detuning between level spacing ω_{10} and the pump microwave, while Ω_{01} is the coupling Rabi frequency, which is proportional to the amplitude of the pump microwave. In contrast to the original value ω_{01}, the magnitude of energy

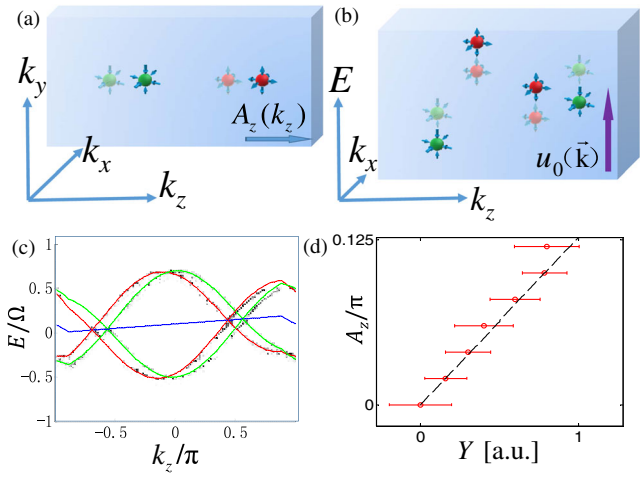

FIG. 3. Effects of an offset A_z and momentum-dependent u_0 are illustrated in (a) and (b). (c) Spectrum along the k_z direction for Hamiltonian in Eq. (1) for $u_0(\mathbf{k}) = f(k_z)\cos(k_x)\cos(k_y)$ (blue line) with $k_x = k_y = 0$, where $f(k_z)$ is given in Eq. (3) with $\alpha = 1$. The vector potential A_z, which causes the shift of the spectrum, is 0 (green) and $\pi/8$ (red), respectively. (d) Plot of A_z as a function of Y. Error bars are derived from the width of resonant peaks in the spectrum.

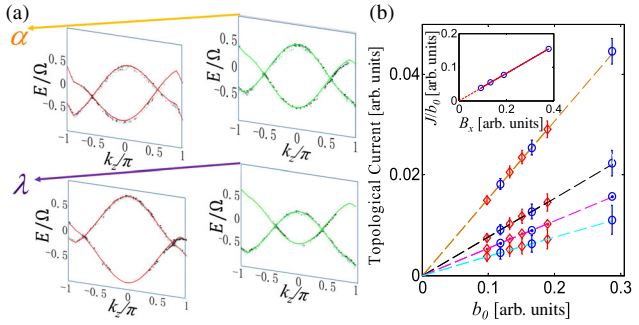

FIG. 4. (a) Energy spectrum with various b_0 obtained by changing λ and u_0. The upper panel shows the spectrum for different α of u_0 with $\lambda = 0$: $\alpha = 1$ (green) and $\alpha = 3$ (red). The lower panel shows the spectrum for $\lambda = 0.5$ (red) and -0.5 (green) with $\alpha = 1$. Solid dots and lines are experimental data and theoretical calculations, respectively. (b) The total topological current derived from Eq. (2), which is contributed to by all four pairs of Weyl points, is plotted as a function of b_0 for various B_x. From bottom to top, B_x is 0.09, 0.13, 0.19, and 0.38, respectively. Blue and red circles are experimental data obtained from the shifts of λ and α, respectively, while dashed lines are theoretical results. The inset of (b) shows the normalized topological current J/b_0 as a function of B_x for the two methods.

shift is $\Delta_{01}/4 + 3\sqrt{\Delta_{01}^2 + \Omega_{01}^2}/4$, which can be accurately controlled by adjusting the amplitude and frequency of pump microwaves. For instance, using an accurately designed waveform, we could obtain a special kind of

$$u_0(\mathbf{k}) = f(k_z)\cos(k_x)\cos(k_y), \tag{3}$$

where $f(k_z)$ is a 2π-periodic function of k_z, which can be set as $f(k_z) = \alpha k_z/(10\pi)$ for $|k_z| \le 7\pi/8$, while $f(k_z) = -7\alpha/10\pi[k_z - \mathrm{sgn}(k_z)]$ for $7\pi/8 \le |k_z| \le \pi$ in the range of $[-\pi, \pi]$, with α being a preset parameter. In our experiments, $f(k_z)$ in the range $[-7\pi/8, 7\pi/8]$ is a simple linear function of k_z, which can generate the energy difference u_0 of a relevant pair of Weyl points. The function in $[-\pi, -7\pi/8)$ and $(7\pi/8, \pi]$ is chosen to have the periodical boundary condition. In Fig. 3(b), we show an example of u_0 with $k_x = k_y = 0$, $\alpha = 1$. Notably, our specific choice of the $\cos(k_x)\cos(k_y)$ term in u_0 is to ensure that the total current contributed from four pairs of Weyl points is 4 times that for a single pair.

We now turn to the second factor of CME. From Eq. (2), the CME topological current will be proportional to both b_0 and the magnetic field $\mathbf{B}$. Since $\mathbf{B} = \nabla \times \mathbf{A}$, we can introduce an artificial vector potential $\mathbf{A}$ to generate the artificial magnetic field needed. Without loss of generality, we assumed that $\mathbf{B}$ was along the x direction and $\mathbf{A}$ had only the z component, such that $B_x = \partial A_z/\partial Y$, where a set of A_z in our experiment was chosen to be proportional to a fictitious coordinate Y (with the dimensionality of length). Considering the form of the canonical momentum, we can introduce the vector potential by adding a controllable shift on the momentum k_z, namely, we transformed k_z to $k_z + A_z$ in the σ_z prefactor of Eq. (1), resulting in $\Omega_3/2 = \Omega[\lambda + \cos(k_z + A_z)]$. In the presence of this offset, the artificial magnetic field may be introduced to act on e-charge single particles. In order to extract B_x, we here adopted a scenario of fictitious work to evaluate $\partial A_z/\partial Y$ from our experimental data. Since we had a good linear momentum-dependent shift of the energy bands near the Weyl points, a small change of A_z will cause an energy difference in ΔE, i.e., $\Delta E \propto \Delta A_z$ near the Weyl points. On the other hand, we may write $\Delta E = F_Y \Delta Y$ near one Weyl point, where F_Y could be viewed as a constant fictitious force acting on the particle which moved ΔY along the Y direction. Therefore, $\Delta A_z \propto \Delta Y$, with the prefactor defining the magnitude of B_x. In our experiments, by choosing various small A_z near the Weyl point, we measured the corresponding ΔA_z and ΔE (i.e., ΔY if we set $F_Y = 1$ force unit). By plotting A_z as a function of Y, we indeed observed a good linear relation, whose slope may approximately give the artificial field B_x. For various fixed B_x, we measured b_0, from which we were able to determine the virtual CME topological current $\mathbf{J}_{\mathrm{topo}}$ based on our derived Eq. (2).

One advantage for simulating topological band structures by using a superconducting transmon is the full controllability of the parameter space. We can continuously tune parameters λ, A_z, and $u_0(\mathbf{k})$ in Eq. (1). We have two ways to vary the virtual CME topological current derived from Eq. (2). One is to change λ. The other is to tune the slope of $u_0(\mathbf{k})$. As indicated in Fig. 4(a), with λ varying from 0.5 to -0.5 for $\alpha = 1$, the energy difference changes from 0.0813 GHz (green) to 0.1512 GHz (red). On the other hand, when k_z is in the range of $(-7\pi/8, 7\pi/8)$, changing the slope

of $f(k_z)$ (i.e., α) in $u_0(\mathbf{k})$ also modifies the energy difference of two Weyl points for a fixed $\lambda = 0$: the energy difference is 0.151 GHz for $\alpha = 1$ (green), while it is 0.430 GHz for $\alpha = 3$ (red). Both methods effectively changed b_0, and hence the virtual topological current. For various B_x, we plotted the topological currents against b_0 for both methods. The currents extracted from the two approaches fall on one straight line for the same B_x, as shown in the main panel of Fig. 4(b). Moreover, the normalized topological current J/b_0 for two different methods depends solely on B_x, as seen from the inset of Fig. 4(b). Finally, we wish to reiterate that the currents addressed here are virtual and not realistic ones for our single-qubit system, and particularly they just reflect the deformational response of the topological band structure to magnetic fields, which are determined from Eq. (2) by measuring b_0.

In summary, our work presents the first experimental report on quantum simulation and manipulation of highly tunable Weyl-semimetal band structures using superconducting qubits, paving the way for further exploration and simulation of topological physics.

This work was partially supported by the NKRDP of China (Grant No. 2016YFA0301802), NSFC (Grants No. 61521001, No. 11504165, No. 11474152, No. 11890704), and the GRF of Hong Kong (Grants No. HKU173055/15P and No. HKU173057/17P).

*hfyu@nju.edu.cn
†zwang@hku.hk
‡yuyang@nju.edu.cn

[1] S. Y. Xu *et al.*, Discovery of a Weyl fermion semimetal and topological Fermi arcs, Science **349**, 613 (2015).
[2] B. Q. Lv, H. M. Weng, B. B. Fu, X. P. Wang, H. Miao, J. Ma, P. Richard, X. C. Huang, L. X. Zhao, G. F. Chen, Z. Fang, X. Dai, T. Qian, and H. Ding, Experimental Discovery of Weyl Semimetal TaAs, Phys. Rev. X **5**, 031013 (2015).
[3] Y. X. Zhao and Z. D. Wang, Disordered Weyl Semimetals and Their Topological Family, Phys. Rev. Lett. **114**, 206602 (2015).
[4] D. T. Son and B. Z. Spivak, Chiral anomaly and classical negative magnetoresistance of Weyl metals, Phys. Rev. B **88**, 104412 (2013).
[5] H.-J. Kim, K.-S. Kim, J.-F. Wang, M. Sasaki, N. Satoh, A. Ohnishi, M. Kitaura, M. Yang, and L. Li, Dirac Versus Weyl Fermions in Topological Insulators: Adler-Bell-Jackiw Anomaly in Transport Phenomena, Phys. Rev. Lett. **111**, 246603 (2013).
[6] X. Huang, L. X. Zhao, Y. J. Long, P. P. Wang, D. Chen, Z. H. Yang, H. Liang, M. Q. Xue, H. M. Weng, Z. Fang, X. Dai, and G. F. Chen, Observation of the Chiral-Anomaly-Induced Negative Magnetoresistance in 3D Weyl Semimetal TaAs, Phys. Rev. X **5**, 031023 (2015).
[7] J. Xiong, S. K. Kushwaha, T. Liang, J. W. Krizan, M. Hirschberger, W. D. Wang, R. J. Cava, and N. P. Ong, Evidence for the chiral anomaly in the Dirac semimetal Na_3Bi, Science **350**, 413 (2015).
[8] C.-Z. Li, L. X. Wang, H. W. Liu, J. Wang, Z. M. Liao, and D. P. Yu, Giant negative magnetoresistance induced by the chiral anomaly in individual Cd_3As_2 nanowires, Nat. Commun. **6**, 10137 (2015).
[9] K. Fukushima, D. E. Kharzeev, and H. J. Warringa, Chiral magnetic effect, Phys. Rev. D **78**, 074033 (2008).
[10] D. E. Kharzeev, The chiral magnetic effect and anomaly-induced transport, Prog. Part. Nucl. Phys. **75**, 133 (2014).
[11] A. A. Zyuzin and A. A. Burkov, Topological response in Weyl semimetals and the chiral anomaly, Phys. Rev. B **86**, 115133 (2012).
[12] J. Q. You and F. Nori, Atomic physics and quantum optics using superconducting circuits, Nature (London) **474**, 589 (2011).
[13] J. Clarke and F. K. Wilhelm, Superconducting quantum bits, Nature (London) **453**, 1031 (2008).
[14] M. D. Schroer, M. H. Kolodrubetz, W. F. Kindel, M. Sandberg, J. Gao, M. R. Vissers, D. P. Pappas, A. Polkovnikov, and K. W. Lehnert, Measuring a Topological Transition in an Artificial Spin-1/2 System, Phys. Rev. Lett. **113**, 050402 (2014).
[15] P. Roushan *et al.*, Observation of topological transitions in interacting quantum circuits, Nature (London) **515**, 241 (2014).
[16] V. Gritsev and A. Polkovnikov, Dynamical quantum Hall effect in the parameter space, Proc. Natl. Acad. Sci. U.S.A. **109**, 6457 (2012).
[17] X. S. Tan, Y. X. Zhao, Q. Liu, G. M. Xue, H. F. Yu, Z. D. Wang, and Y. Yu, Realizing and manipulating space-time inversion symmetric topological semimetal bands with superconducting quantum circuits, npj Quantum Mater. **2**, 60 (2017).
[18] X. S. Tan, D.-W. Zhang, Q. Liu, G. M. Xue, H.-F. Yu, Y.-Q. Zhu, H. Yan, S.-L. Zhu, and Y. Yu, Topological Maxwell Metal Bands in a Superconducting Qutrit, Phys. Rev. Lett. **120**, 130503 (2018).
[19] H. Paik, D. I. Schuster, L. Bishop, G. Kirchmair, G. Catelani, A. Sears, B. R. Johnson, M. Reagor, L. Frunzio, and L. I. Glazman, Observation of High Coherence in Josephson Junction Qubits Measured in a Three-Dimensional Circuit QED Architecture, Phys. Rev. Lett. **107**, 240501 (2011).
[20] J. Q. You and F. Nori, Quantum information processing with superconducting qubits in a microwave field, Phys. Rev. B **68**, 064509 (2003).
[21] X. Gu, A. F. Kockum, A. Miranowicz, Y. X. Liu, and F. Nori, Microwave photonics with superconducting quantum circuits, Phys. Rep. **718–719**, 1 (2017).
[22] A. Blais, R. S. Huang, A. Wallraff, S. M. Girvin, and R. J. Schoelkopf, Cavity quantum electrodynamics for superconducting electrical circuits: An architecture for quantum computation, Phys. Rev. A **69**, 062320 (2004).
[23] A. Wallraff, D. I. Schuster, A. Blais, L. Frunzio, R.-S. Huang, J. Majer, S. Kumar, S. M. Girvin, and R. J. Schoelkopf, Strong coupling of a single photon to a superconducting qubit using circuit quantum electrodynamics, Nature (London) **431**, 162 (2004).
[24] See Supplemental Material at http://link.aps.org/supplemental/10.1103/PhysRevLett.122.010501 for details of the experimental setup, measurement procedures, and data analysis, which includes Refs. [19,25–29].

[25] M. Steffen, M. Ansmann, R. McDermott, N. Katz, R. C. Bialczak, E. Lucero, M. Neeley, E. M. Weig, A. N. Cleland, and J. M. Martinis, State Tomography of Capacitively Shunted Phase Qubits with High Fidelity, Phys. Rev. Lett. **97**, 050502 (2006).

[26] E. T. Jaynes and F. W. Cummings, Comparison of quantum and semiclassical radiation theories with application to the beam maser, Proc. IEEE **51**, 89 (1963).

[27] M. A. Sillanpaa, J. Li, K. Cicak, F. Altomare, J. I. Park, R. W. Simmonds, G. S. Paraoanu, and P. J. Hakonen, Autler-Townes Effect in a Superconducting Three-Level System, Phys. Rev. Lett. **103**, 193601 (2009).

[28] B. R. Mollow, Power spectrum of light scattered by two-level systems, Phys. Rev. **188**, 1969 (1969).

[29] M. Baur, S. Filipp, R. Bianchetti, J. M. Fink, M. Göppl, L. Steffen, P. J. Leek, A. Blais, and A. Wallraff, Measurement of Autler-Townes and Mollow Transitions in a Strongly Driven Superconducting Qubit, Phys. Rev. Lett. **102**, 243602 (2009).

[30] M. D. Reed, L. DiCarlo, B. R. Johnson, L. Sun, D. I. Schuster, L. Frunzio, and R. J. Schoelkopf, High-Fidelity Readout in Circuit Quantum Electrodynamics Using the Jaynes-Cummings Nonlinearity, Phys. Rev. Lett. **105**, 173601 (2010).

[31] See Supplemental Material at http://link.aps.org/supplemental/10.1103/PhysRevLett.122.010501 for the equation derivation, which includes Refs. [11,32].

[32] K. Fujikawa, Path-Integral Measure for Gauge-Invariant Fermion Theories, Phys. Rev. Lett. **42**, 1195 (1979).

[33] H. B. Nielsen and M. Ninomiya, A no-go theorem for regularizing chiral fermions, Phys. Lett. B **105**, 219 (1981).

[34] M. M. Vazifeh and M. Franz, Electromagnetic Response of Weyl Semimetals, Phys. Rev. Lett. **111**, 027201 (2013).